

UNIVERSITY OF TARTU

Faculty of Science and Technology

Institute of technology

Xueran Tao

Maximum packing density of ions at ionic liquid–electrode interfaces

Bachelor's thesis in Chemistry (12 ECTS)

Supervisor: PhD Vladislav Ivaništšev

Tartu 2022

# Maximum packing density of ions at ionic liquid–electrode interfaces

## ABSTRACT

In this work, we have developed a workflow for simulating a one electrode model of ionic liquid–electrode interfaces (ILEIs). The workflow utilises Packmol to generate the initial models, Gromacs to run and process molecular dynamics simulations, and python scripts to evaluate the maximum packing density ( $\theta_M$ ) of the contact layer at the ILEI. By these means, we have studied 40 ionic liquid ions with a focus on the monolayer structure formation and surface charge screening. Based on the differences in the screening mechanism, we divided all ions into four classes: balls, roly-poly, teeter-totter, and head-tail. Using the obtained  $\theta_M$  and geometric values, we have estimated structure-determined potential and capacitance values. By comparing the predictions to the empirical data, we conclude that for the studied ILEIs the monolayer formation is impossible within the measurable potential window. Finally, we have suggested ions that potentially can exhibit the monolayer formation within their electrochemical window.

**CERCS:** P352, P401

**Keywords:** ionic liquids, molecular dynamics simulations, maximum packing density, electrical double layer, overscreening, crowding, interface.

# Ioonide maksimaalne pakkimise tihedus ioonvedeliku ja elektroodi piirpindadel

## LÜHIKOKKUVÕTE

Käesolevas töös oleme välja töötanud töövoos ioonvedeliku–elektroodi piirpindade (ILEI) ühe elektroodse mudeli simuleerimiseks. Töövoog kasutab Packmol'i esialgsete mudelite koostamiseks, Gromacs'i molekulaardünaamika simulatsioonide käivitamiseks ja töötlemiseks ning Python-skripte, et hinnata ILEI kontaktkihi maksimaalset pakkimise tihedust ( $\theta_M$ ). Nende vahenditega oleme uurinud 40 ioonvedeliku iooni, keskendudes monokihi struktuuri moodustumisele ja pinnalaengu varjamisele. Varjumismehhanismi erinevuste põhjal jagasime kõik ioonid nelja klassi: pallid, jonnipunnid, kiigud ja pea-saba. Kasutades saadud  $\theta_M$  ja geomeetrilisi väärtusi, oleme hinnanud struktuurist tingitud potentsiaali ja mahtuvuse väärtusi. Võrreldes ennustatud väärtusi empiiriliste andmetega, järeldame, et uuritud ILEIde puhul on monokihi moodustumine võimatu mõõdetava potentsiaali aknas. Lõpuks pakkusime välja ioonid, mille elektrokeemilises aknas võib potentsiaalselt tekkida monokiht.

**CERCS:** P352, P401

**Võtmesõnad:** ioonsed vedelikud, molekulaardünaamika, maksimaalne pakkimise tihedus, elektriline kaksikkiht, ülevarjestamine, tunglemine, piirpind

# CONTENTS

<b>1. List of abbreviations and notation used</b>	<b>5</b>
2. Introduction	6
<b>3. Literature overview</b>	<b>7</b>
3.1. Theoretical models	7
3.2. Computer modelling	10
<b>4. Methods</b>	<b>12</b>
4.1. Approach	12
4.2. Simulations	12
4.3. Workflow	13
4.4. Analysis	13
4.4.1. Maximum packing density	13
4.4.2. Monolayer potential drop	14
4.4.3. Structure-determined potential drops and capacitances	15
<b>5. Results</b>	<b>16</b>
5.1. Ball class	16
5.2. Head-tail class	17
5.3. Roly-poly class	19
5.4. Teeter-totter class	21
5.5. Summary of results	22
<b>6. Discussions</b>	<b>24</b>
6.1. Comparison of structure-determined potentials	24
6.2. Ion shape and the monolayer potential	25
6.3. Concluding remarks and future research directions	25
<b>7. Summary</b>	<b>26</b>
<b>8. References</b>	<b>27</b>
<b>9. Appendices</b>	<b>34</b>
9.1. Table 1. Nomenclature names and acronyms of all simulated ions	34
9.2. Table 2. Structure-determined parameters of the modelled ILEIs with head-tail ions	35
NON-EXCLUSIVE LICENCE TO REPRODUCE THESIS AND MAKE THESIS PUBLIC	36

## 1. LIST OF ABBREVIATIONS AND NOTATION USED

CDFT	Classical Density Functional Theory
EDL	Electrical Double Layer
IBL	Interfacial Bilayer Model
IL	Ionic Liquid
ILEI	Ionic liquid electrochemical interface
MD	Molecular dynamics
MC	Monte Carlo
NaRIBaS	Nanomaterials and Room-temperature ILs in Bulk and Slab
PZC	Potential of Zero Charge
$C$	differential capacitance
$C_M$	capacitance of the monolayer
$C_S$	capacitance of the saturated interface
$\Delta\phi$	potential drop across the interface
$\Delta\phi_M$	potential drop across the monolayer
$\Delta\phi_S$	potential drop across the saturated interface
$\sigma$	surface charge density
$l$	distance between the surface charge density and the electrolyte charge density planes; distance between the surface and contact layer
$l_M$	distance between the surface charge density and the monolayer charge density planes; distance between monolayer and the electrode surface
$\theta$	charge density of the contact layer
$\theta_M$	maximum packing density corresponding to the monolayer

## 2. INTRODUCTION

The potential of using ionic liquids (ILs) in technological applications motivates extensive studies of IL–electrode interfaces (ILEIs). Remarkable advances have been reached in the experimental characterisation of such interfaces. Namely, the unique layering of ions near the electrode surface (known as *overscreening*) was accessed with an impressively wide range of spectroscopy [1–15], microscopy [16–28], and electrochemistry techniques [29–43]. Moreover, the theoretically predicted *crowding* of counter-ions [44–47] was observed in computer simulations [48–53]. Kirchner *et al.* identified in simulations a transitional overscreening-to-crowding structure that corresponds to the maximum density of ions ( $\theta_M$ ) packed in a monolayer of counter-ions [51]. At the potential of the monolayer formation, the surface charge density ( $\sigma$ ) is completely screened by the contact layer of ions ( $\sigma = -\theta_M$ ). That monolayer Ansatz was developed in further works [54–56] and appeared in various molecular dynamics (MD), Monte Carlo (MC), and classical density functional theory (CDFT) studies [50,52,57]. However, neither crowding nor monolayer formation have been decisively demonstrated in experiments [12,13,15,40,41,58].

We hypothesise that predicting the  $\theta_M$  values can guide the experimental characterization of crowded ILEIs as well as the estimation of structure-determined ILEI properties. Since the near-surface structure of an IL affects, for example, the heterogeneous electron transfer, the interfacial capacitance, and interfacial lubricity, then estimating the  $\theta_M$  values is presumably of great practical importance.

Previously,  $\theta_M$  values were evaluated for a set of ions in work [59]. That study concluded that observation of the monolayer structure for ions of practical importance ( $\text{Im}_4^+$ ,  $\text{TFSI}^-$ ,  $[\text{FEP}]^-$ ) is unlikely under experimental conditions due to very high estimated potential drop across the monolayer ( $\Delta\phi_M$ ). In this work, with the help of MD simulations, we took the next step to calculate  $\theta_M$  and  $\Delta\phi_M$  values for a larger set of ions with different sizes and shapes. All studied ions are listed in the Appendix Table 1 and their ball-and-stick visualisation is shown in [Figure 1](#).

This BSc project aimed to (1) develop a workflow for efficient density estimation of an ionic monolayer at an oppositely charged surface, and (2) test the workflow on common IL ions to obtain  $\theta_M$  values and related structure-determined potential and capacitance values.

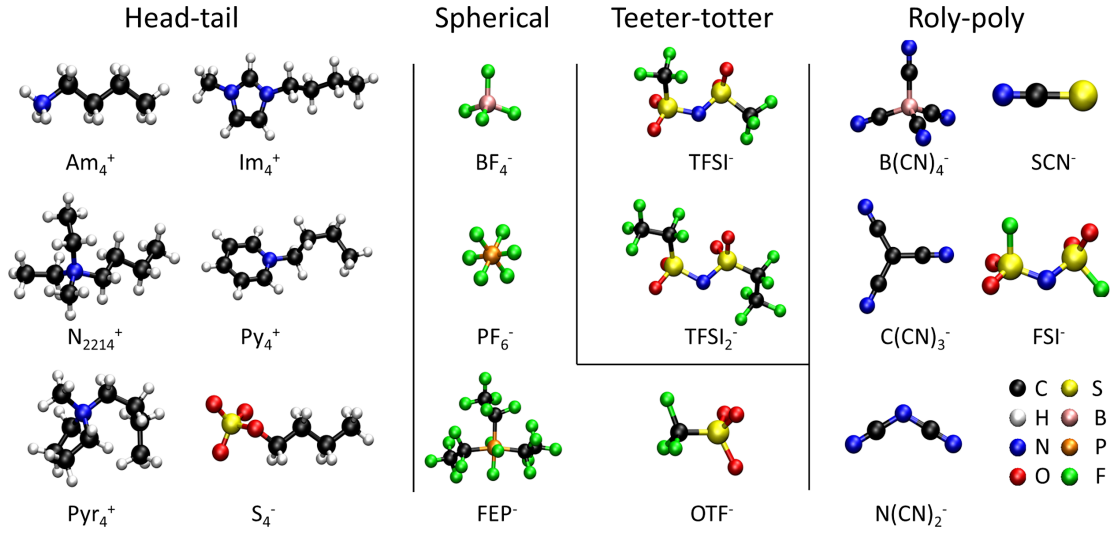


Figure 1: Ball-and-stick model of selected ions representing four identified classes. For ion names and acronyms see the Appendix Table 1.

### 3. LITERATURE OVERVIEW

#### 3.1. Theoretical models

At an atomically flat surface, the electrical double layer (EDL, *i. e.*, interfacial structure) represents a parallel plate capacitor with a charge density ( $\sigma$ ) and a potential drop between the two plates ( $\Delta\varphi$ ). One charge plane is given by the electron charge density distribution at the surface while the other charge plane is given by the ion charge density distribution of the electrolyte ions at the interface. The so-called Helmholtz model (see Ref. [60]) is the simplest model of the EDL, postulating that a charged surface attracts ions of the opposite charge to form a layer of these counter-ions. In this model, the surface charge density plane is set at the nuclei position of the outer surface atoms, while the electrolyte charge density plane is set at the nuclei position of the counter-ion layer ions. In other words, the charge density distributions are expressed *via* the geometric structure parameters of the interface. Assuming that the distance between the surface and ion layers ( $l_H$ ) is constant, the Helmholtz capacitance ( $d\sigma/d\Delta\varphi$ ) is given as:

$$C_H = \frac{\varepsilon_r \varepsilon_0}{l_H} \quad (1)$$

where  $\varepsilon_r$  and  $\varepsilon_0$  stand for the relative permittivity and the permittivity of vacuum.

For diluted aqueous electrolytes, Gouy and Chapman introduced a diffuse layer [61], which accounted for the thermal motion of ions that prevented them from simply

accumulating at the surface and considered them distributed in a larger space. Such modification gives an expression that qualitatively describes the capacitance of low absolute potentials:

$$C_{GC} = \frac{\varepsilon_r \varepsilon_0}{l_D} \cosh\left(\frac{F\Delta\phi}{2RT}\right) \quad (2)$$

where  $l_D$  is the concentration-dependent Debye length,  $F$  is the Faraday constant,  $R$  is the gas constant, and  $T$  is temperature.

For concentrated ILs, Kornyshev introduced the ratio of the bulk density of the ions in the liquid to the maximum possible density in the double layer ( $\gamma$ ) [62] and a short-range correlations parameter ( $\alpha$ ) [63]. At  $\gamma = 0$  and  $\alpha = 1$ , that model reduces to the Gouy–Chapman model. At  $0 < \gamma < 1$  and  $0 < \alpha < 1$ , that model qualitatively describes two common capacitance–potential dependencies known as bell shape and camel shape:

$$C_K = \frac{\varepsilon_r \varepsilon_0}{l_D} \frac{\sqrt{\alpha} \cosh\left(\alpha \frac{F\Delta\phi}{2RT}\right)}{1 + 2\gamma \sinh^2\left(\alpha \frac{F\Delta\phi}{2RT}\right)} \sqrt{\frac{2\gamma \sinh^2\left(\alpha \frac{F\Delta\phi}{2RT}\right)}{\ln\left[1 + 2\gamma \sinh^2\left(\alpha \frac{F\Delta\phi}{2RT}\right)\right]}} \quad (3)$$

Both Gouy–Chapman and Kornyshev models must account for the distance of the closest approach as suggested by Stern [4], which effectively imply adding in series the Helmholtz capacitance as:

$$\frac{1}{C_{EDL}} = \frac{1}{C_H} + \frac{1}{C_{GC/K}} \quad (4)$$

Depending on the electrolyte the contact layer charge density ( $\theta$ ) is either higher or lower than needed to compensate for the surface charge density ( $\sigma$ ) by:

$$\lambda = -(\sigma + \theta) \quad (5)$$

In Ref. [55] the quantity  $\lambda$  is referred to as the surface charge excess regarding ILEI where the contact layer overscreens the surface charge. That quantity is compensated by the charge of the subsequent EDL layers in ILs or of the diffuse layer in aqueous solutions. In the case of ILEI, it is justified to relate  $\lambda$  to the geometric structure as the Debye length in ILs is

comparable to the size of ions. For example, the interfacial bilayer model (IBL) [56] assumes that the first two ion layers determine the potential drop as:

$$\Delta\varphi = \frac{l\sigma - \delta\lambda}{\varepsilon_r\varepsilon_0} \quad (6)$$

where  $l$  and  $\delta$  are the distances between the electrode and the contact layer and between the contact and second layer. For potential ranges of interest, it is reasonable to assume independence of  $l$  and  $\delta$  of  $\Delta\varphi$ , so that the capacitance can be expressed as:

$$C_{\text{IBL}} = \frac{\varepsilon\varepsilon_0}{l} + \frac{\delta}{l} \frac{\partial\lambda}{\partial\Delta\varphi} \quad (7)$$

where the first term is the Helmholtz capacitance ( $C_{\text{H}}$ ) from Eq. (1).

Based on MD simulation results, Voroshylova *et al.* related the saturation of the second layer to the condition  $\partial\lambda/\partial\Delta\varphi = 0$  at which the IBL capacitance equals  $C_{\text{H}}$  [56]:

$$C_{\text{S}} = C_{\text{H}} \quad (8)$$

Previously, with the help of MD simulations Kirchner *et al.* observed the saturation of the contact layer – the monolayer formation [51]. Assuming Helmholtz like charging, the monolayer capacitance equals [65]:

$$C_{\text{M}} = \frac{l_{\text{M}}}{l_{\text{M}} + \delta_{\text{M}}} C_{\text{H}} = aC_{\text{H}} \quad (9)$$

where  $l_{\text{M}}$  and  $\delta_{\text{M}}$  are the distances between the electrode and the monolayer layer and between the monolayer and second layer in the crowding regime. Furthermore, the charge conservation law [62,66], can be used for the estimation of  $C(\Delta\varphi)$  dependence around  $\Delta\varphi_{\text{M}}$ :

$$C = aC_{\text{H}} \left( \frac{\Delta\varphi}{\Delta\varphi_{\text{M}}} \right)^{a-1} \quad (10)$$

Equalising Eqs. (8)–(9) to Eq. (10) gives the structure-determined potentials [67]:

$$\Delta\varphi_S = \frac{\theta_M}{C_H} \left( \frac{1}{a} \right)^{\frac{1}{a-1}} \quad (11)$$

and

$$\Delta\varphi_M = \frac{\theta_M}{C_H} \quad (12)$$

In the work, we evaluated  $\theta_M$  and estimated  $(C_M, \Delta\varphi_M)$  and  $(C_S, \Delta\varphi_S)$  for each ion using Eqs (8)–(12).

### 3.2. Computer modelling

Although nowadays there are many theories for ILEI properties [45–47,62,63,68–70], few of them and only in the most general manner reproduce the key ILEI structural features such as overscreening and crowding. Computer modelling performs this task much better and, thus, provides a better ground for a phenomenological understanding of the ILEI.

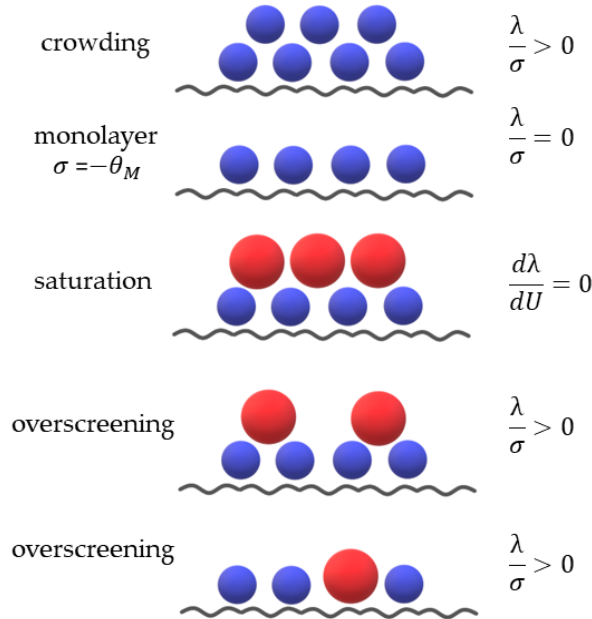


Figure 2: Schematic representation of an ionic liquid–electrode interface at variable surface charge density that is screened by shown counter- and co-ions. The given criteria are discussed in the text.

Rich structural features and slow dynamics of the ILEI represent a challenge for building computer models and developing theories that can reproduce the ILEI characteristic phenomena of overscreening, monolayer formation, and crowding. [Figure 2](#) illustrates different states observed in MD simulations of the ILEI [46,49,51,56]. The overscreening,

monolayer and crowding are the states at which  $|\sigma| < |\theta|$ ,  $\sigma = -\theta_M$ , and  $|\sigma| > |\theta|$ , respectively. Or, in terms of  $\lambda$  and  $\sigma$ ,  $\lambda/\sigma > 0$  (overscreening),  $\lambda/\sigma = 0$  (monolayer), and  $\lambda/\sigma < 0$  (crowding). [Figure 2](#) shows two types of overscreening: first, with co-ions present in the contact layer and, second, with all co-ions pushed to the second layer. On the one hand, close to the potential of zero charge (PZC), there is a high density of co-ions near the surface. On the other hand, at higher absolute potentials, co-ions are pushed to the second layer and  $\theta$  is determined solely by the density of counter-ions. Finally, the density of co-ions in the second layer also reaches the state of saturation when  $\lambda$  approaches its maximum, *i. e.*,  $d\lambda/d\sigma = 0$ .

Computational modelling allows for atomistic simulations of the EDL in specific ILs in parallel to their experimental characterization. On the one hand, realistically long simulations of large models, especially using quantum mechanics, require enormous high-performance computing resources. On the other hand, simulations focusing on a specific process require simpler models, shortened runs, and fewer resources. The monolayer formation is one of such processes that can be described with the Helmholtz model. Following the simplification approach, we have studied 40 ILs at a model ILEI, which is by an order of magnitude more than in a standard MD simulation work.

## 4. METHODS

### 4.1. Approach

Most of the ILEI simulations are performed with the two electrode model that consists of two electrodes and an IL electrolyte composed of both counter-ions and co-ions [71]. In this work, we used a single electrode ILEI model that includes only counter-ions, i.e. similar to the Helmholtz model. We used that model to evaluate the maximum packing density ( $\theta_M$ ) under the assumption that the monolayer of counter-ions completely screens the surface charge density ( $\sigma = -\theta_M$ ), as reported in the literature [51]. On that basis, we expect our model to give  $\theta_M$  and  $\Delta\phi_M$  values similar to those obtained from more sophisticated two-electrode ILEI models. Herewith, the use of the one electrode model reduces the computational resource demand by two orders of magnitude in comparison to the two electrode models.

### 4.2. Simulations

The electrode was prepared using the Atomic Simulation Environment [72] with a size of 4.262577 nm $\times$ 3.9376 nm (640 carbon atoms). The Packmol algorithm [73] with variable seeds was used to generate five replicas of the ILEI models with counter-ions. The surface charge was set by fixing the atomic charge on each electrode atom. The whole system was kept electroneutral as counter-ions completely compensate for the surface charge.

The GROMACS software package [74–80] was used to perform the simulations. First, the simulation ran for 10 ps with a 1 fs time step using a steep integrator as a rough energy minimization run. Then, ran for 20 ps with a 0.5 fs time step as an equilibration step to generate velocities equivalent to a temperature of 100 K. The final production run lasted 1000 ps, with a 1 fs time step and velocities corresponding to 353 K. The verlet cut-off scheme was employed and *xy*-periodic boundary conditions were applied with the particle-mesh Ewald and 3dc Ewald correction [81–83]. Next, the trajectories excluding the first 10 ps of the production run were analysed. Charge density, mass density, and electrostatic potential profiles were obtained using GROMACS tools and automatically collected and processed with python scripts. And distances were analysed by MDanalysis software [84,85]. Visualisation of the ILEI models and ions was prepared with the VMD software [86].

### 4.3. Workflow

A customizable and automated workflow was built using the NaRIBaS (Nanomaterials and Room-temperature ILs in Bulk and Slab) scripting framework [87]. With the required ion and electrode topology files and defines the input parameters, the NaRIBaS script can be initiated. Then it starts generating systems with predefined numbers of counter-ions near the electrode surface within a box and performs molecular dynamics (MD) simulations. The whole system can remain electroneutral as the electrode is charged oppositely.

The number densities of the counter-ions are extracted from the MD trajectories by a preset and unique “centre” for different ions. The maximum packing density for ions is then determined by observing the dependency of contact layer ion densities on the surface charge densities. Before the contact layer gets crowded, the rise in monolayer density is naturally linear with the surface charge density. The maximum density will then be simulated and shown as a plateau on the graph.

### 4.4. Analysis

#### 4.4.1. *Maximum packing density*

Using the numerical evaluation of the mass density profiles, the contact layer was defined from each ion at each simulated  $\sigma$  value. In the perpendicular direction to the electrode surface, the appearance of the contact layer is defined as the point at which the density in the slice exceeds a threshold, and the end of the contact layer is defined as the point at which the density returns below the threshold. The density of a contact layer ( $\theta$ ) is found by integrating the density in the slices in between. Each  $\theta_M$  value was automatically estimated by plotting  $\theta$  vs  $\sigma$  as illustrated in [Figure 4](#). The estimation precision depends on how much ions reorient with increasing  $\sigma$ . Therefore, we checked for the crowding condition – occurrence of counter-ions in the second layer – to obtain the  $\theta_M$  values reported in the Tables below. In addition, we evaluated  $l_M$  and  $\delta_M$  values for Eq. [\(9\)](#).

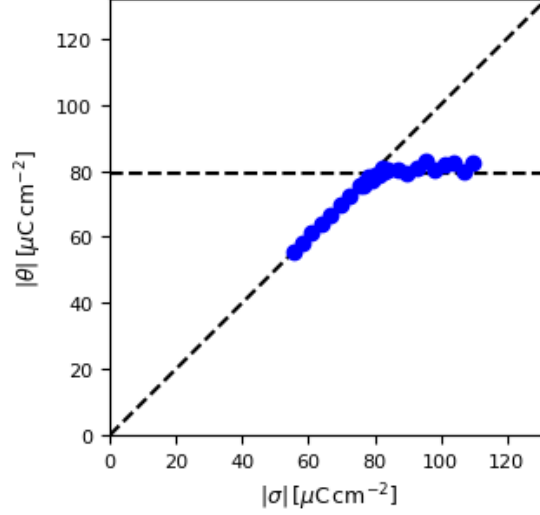


Figure 3: Contact layer charge density ( $\theta$ ) dependence on the surface charge density ( $\sigma$ ) for  $\text{PF}_6^-$ . The maximum packing density ( $\theta_M$ ) corresponds to the plateau.

#### 4.4.2. Monolayer potential drop

The monolayer potential drop ( $\Delta\phi_M$ ) was calculated using the Poisson equation and the charge density profiles. Then we recalculated these values under the assumptions that, firstly, the partial charge transfer can be accounted for by varying relative permittivity ( $\epsilon_r$ ), and, secondly, the total potential drop can be split into electrode and electrolyte contributions.

The first assumption views the partial charge transfer as an extreme on electronic polarisation at the ILEI. In our simulations, we used  $\epsilon_r = 1$ , while values from 1.6 to 2 are commonly used in MD simulations to account for electronic polarisation through atomic charge scaling as  $q = \epsilon_r^{-1/2}$  [88].

The second assumption was tested by comparing  $\Delta\phi_M$  values evaluated (1) directly *via* the Poisson equation, (3) using obtained  $l_M$  in  $\Delta\phi_M = l_M\theta_M/\epsilon_r\epsilon_0$ , and using simulated  $\theta_M$  in the following expression:

$$\Delta\phi_M = -\frac{d+r}{\epsilon_r\epsilon_0}\theta_M = -\frac{d\theta_M}{\epsilon_r\epsilon_0} + k \cdot q \frac{\sqrt{q\theta_M}}{\epsilon_r\epsilon_0} \quad (13)$$

where  $q$  is the counter-ion charge ( $\pm 1e$  in this study),  $k$  is the compression factor of an ion, *i. e.* the ratio between contact ( $r$ ) and the lateral ( $R^2 = 1/4 \cdot q/\theta_M$ ) radii of the counter-ion. The compression factor ( $k = r/R$ ) indicates how much the ion's elliptic form deviates from a

sphere. The summation of  $d$  and  $r$  relies on the assumption that the distance between the surface and the contact layer is given by the radii of surface atoms and counter-ions.

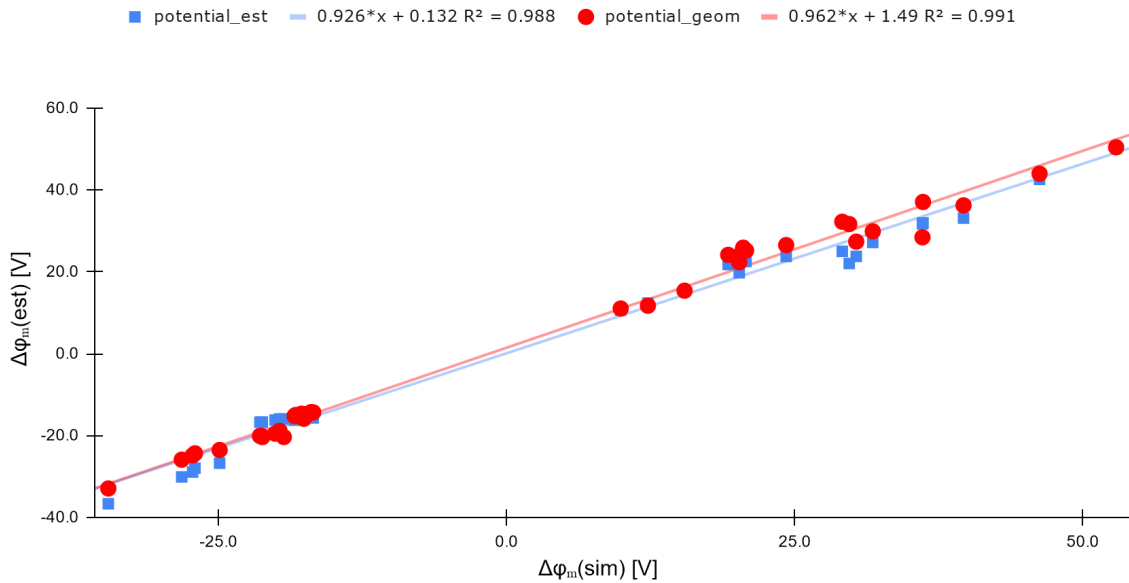


Figure 4: Plot of estimated  $\Delta\phi$  values against  $\Delta\phi_M$  calculated with Poisson equation. Blue points are calculated with Eq. (13). Red points are calculated as  $\Delta\phi_M = l_M\theta_M/\epsilon_r\epsilon_0$ .

Figure 4 demonstrates the high coefficients of determination ( $R^2$ ) of 0.991 and 0.988 for linear regression of (1)–(2) and (1)–(3) values. Indeed, the potential drop within distance ( $d$ ) from the electrode can be associated with the electrode and corrected as described in Ref. [89]. So, below, we set  $d = 0$  nm in Eq. (13) by assuming that the surface charge plane of an ideal metal electrode extends by one-half of an interplanar spacing as follows from theory [90,91] and calculations [92,93].

#### 4.4.3. Structure-determined potential drops and capacitances

As described above, the monolayer potential drop –  $\Delta\phi_M$  – corresponds to the saturation of the contact layer. Another structure-determined potential –  $\Delta\phi_S$  – corresponds to the saturation of the second layer.  $\Delta\phi_M-C_M$  and  $\Delta\phi_S-C_S$  pair values were predicted using Eqs. (8)–(12) with  $l = r_M$  and  $\epsilon_r = 2$ .

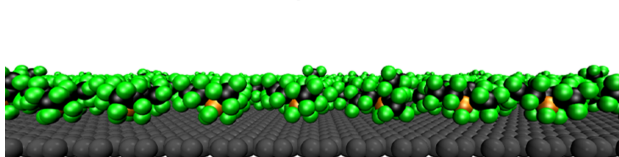
## 5. RESULTS

After the analysis of simulation data, the examined ions were classified into four distinct groups based on their interfacial behaviour: ball, head-tail, roly-poly, and teeter-totter. The interfacial behaviour was differentiated by the  $-\theta(\sigma)$  dependence. The ball and teeter-totter ions give a simple  $|\theta|-\sigma$  plot with two clear intersecting lines, while head-tail and roly-poly groups show more complex  $|\theta|-\sigma$  plots due to the reorientation of individual ions.

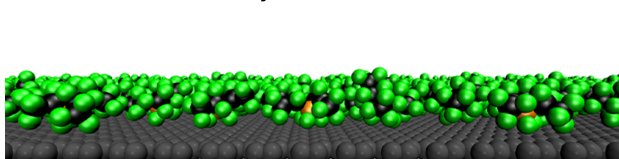
### 5.1. Ball class

The ball class, as its name suggests, includes roundish ions such as  $\text{BF}_4^-$ ,  $\text{Br}^-$ ,  $\text{Cl}^-$ ,  $\text{FEP}^-$ ,  $\text{I}^-$ ,  $\text{OTF}^-$  and  $\text{PF}_6^-$ . Their main feature is that they behave like coarse-grain balls during the simulations and form close-packed structures.

25  $\text{FEP}^-$  ions (contact layer)



27  $\text{FEP}^-$  ions (monolayer)



29  $\text{FEP}^-$  ions (two layers)

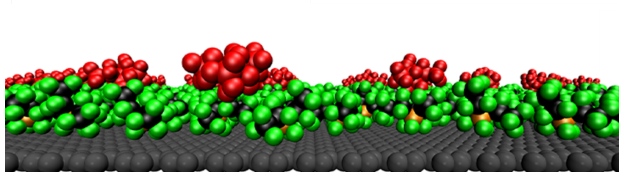


Figure 5: Ball-and-stick models of the  $\text{FEP}^- |$  electrode interface. The maximum packing density is reached in simulations of 27  $\text{FEP}^-$  ball ions per the electrode area. Ions forming the second layer are shown in red.

[Figure 5](#) shows the packing of ball  $\text{FEP}^-$  ions. Due to the simple shape, ions are well organised and fill the surface in a highly ordered manner resulting in dense packing. Ions belonging to this class do not change orientations upon increasing  $|\sigma|$ . However, with  $|\sigma|$  increase, their packing density can increase stepwise.

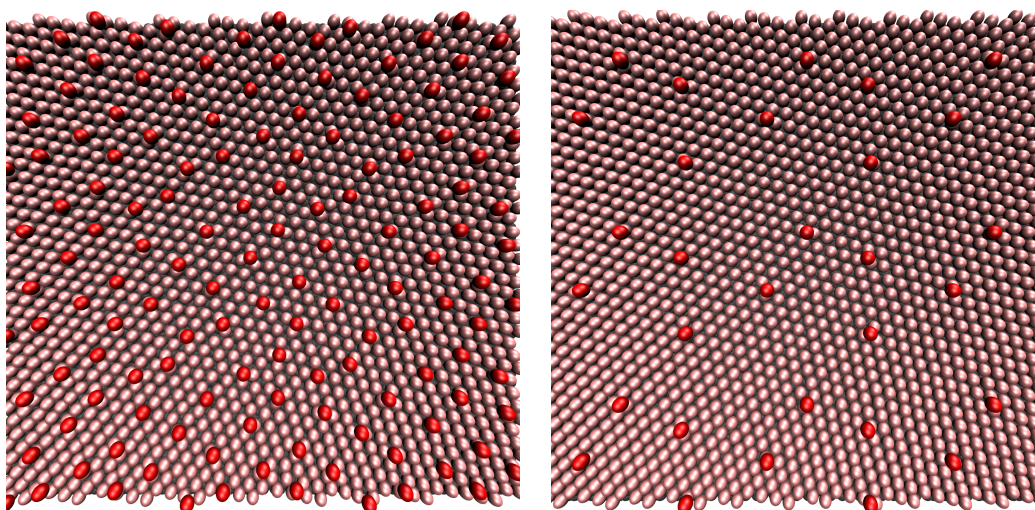


Figure 6: Two dense packings of  $\text{Br}^-$  adlayers. Left: model with 173 ions, 157 of which are in the contact layer. Right: model with 174 ions, 170 of which are in the contact layer.

For example, in [Figure 6](#) the maximum packing density is increasing stepwise from  $-150$  to  $-162 \mu\text{C}\cdot\text{cm}^{-2}$  when  $\sigma$  is increased by only  $1 \mu\text{C}\cdot\text{cm}^{-2}$ . A similar phenomenon is well known for halide anions adsorbing from aqueous solutions [94]. Most recently, analogues stepwise densening was observed in MD simulations of  $\text{BMImPF}_6 | \text{Au}(hkl)$  interfaces [65].

[Table 1](#) summarises simulated and estimated parameters of the modelled ILEIs with ball ions. This data is discussed below.

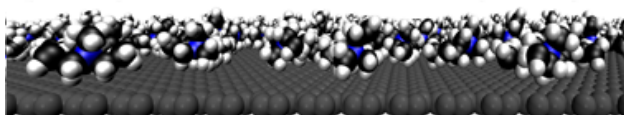
Table 1: Structure-determined parameters of the modelled ILEIs with ball ions.

Ion	$\theta_M [\mu\text{C}\cdot\text{cm}^{-2}]$	$\varphi_M [\text{V}]$	$\varphi_S [\text{V}]$	$C_M [\mu\text{F}\cdot\text{cm}^{-2}]$	$C_S [\mu\text{F}\cdot\text{cm}^{-2}]$	$a$
$\text{BF}_4^-$	-105.95	10.5	1.9	3.1	10.1	0.60
$\text{Br}^-$	-149.85	9.5	1.5	4.0	15.7	0.26
$\text{Cl}^-$	-182.30	9.7	1.5	4.4	18.9	0.23
$\text{FEP}^-$	-25.77	3.8	0.8	2.5	6.7	0.71
$\text{I}^-$	-86.86	7.4	1.2	3.0	11.8	0.26
$\text{OTF}^-$	-73.49	7.8	1.2	2.2	9.4	0.39
$\text{PF}_6^-$	-78.27	10.8	2.2	2.6	7.3	0.60

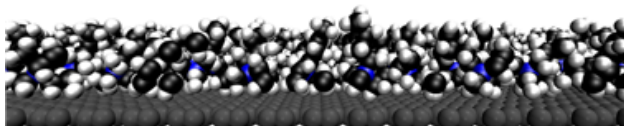
## 5.2. Head-tail class

Head-tail ions consist of an alkyl chain tail and a head. For  $\text{Py}_n^+$  and  $\text{Im}_n^+$  the head is an aromatic cycle. For  $\text{Am}_n^+$ ,  $\text{Pyr}_n^-$  and  $\text{N}_{2214}^+$  ions, the head is an (alkyl)ammonium group.

15  $N_{2214}^+$  ions (contact layer)



46  $N_{2214}^+$  ions (monolayer)



57  $N_{2214}^+$  ions (two layers)

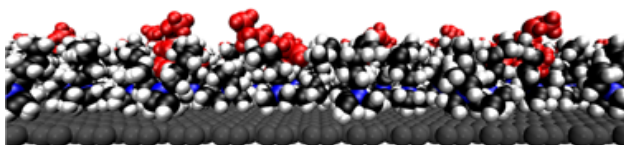
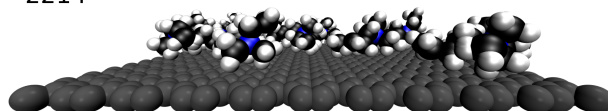


Figure 7: Ball-and-stick model of  $N_{2214}^+$  | electrode interface from the head-tail ions. The maximum packing density is reached in simulations of 46  $N_{2214}^+$  ions at the electrode model. Ions of the second layer are shown in red.

Head-tail ions demonstrate parallel and perpendicular orientations depending  $|\sigma|$ . For both orientations, ion heads are in contact with the surface as they hold the charges while tails occupy available space at or above the surface. [Figure 7](#) shows the packing of head-tail  $N_{2214}^+$  cation with reorientation and crowding.

$N_{2214}^+$  ions flat orientation



$N_{2214}^+$  ions standing orientation

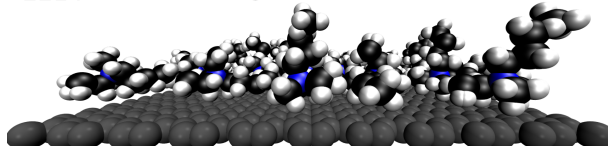


Figure 8: Ball-and-stick model of  $N_{2214}^+$  | electrode interface. Changes in the tail orientation from parallel to perpendicular to the surface.

As shown in [Figure 8](#), when there is enough space at the surface, ions orient parallel, *i. e.*, tails lie down and directly touch the surface. When the number of ions on the surface increases, tails are forced to stand up. This phenomenon was previously reported in many

simulation works, *e. g.* [13]. At the maximum packing density, all tails at all studied ILEIs were standing. Aromatic rings in  $\text{Im}_n^+$  and  $\text{Py}_n^+$  ions also change orientation from parallel to perpendicular relative to the surface upon increasing  $|\sigma|$ . Some aspects of such reorientation are discussed in Refs. [2,95,96]. This study reveals that in the monolayer structure only a small fraction of ring heads, unlike tails, is in the perpendicular orientation.

[Table 2](#) summarises simulated and estimated parameters of the modelled ILEIs with head-tail ions with the tail length of 4. Additional data is given in Appendix Table 2.

Table 2: Structure-determined parameters of the modelled ILEIs with head-tail ions. Only one set is shown per each family of ions, while more detailed data is given in Appendix 2 Table 2.

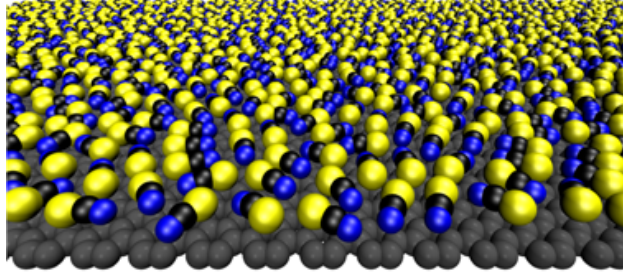
Ion	$\theta_M [\mu\text{C}\cdot\text{cm}^{-2}]$	$\varphi_M [\text{V}]$	$\varphi_S [\text{V}]$	$C_M [\mu\text{F}\cdot\text{cm}^{-2}]$	$C_S [\mu\text{F}\cdot\text{cm}^{-2}]$	$a$
$\text{Am}_4^+$	98.31	-4.4	-1.2	13.5	22.5	0.60
$\text{Im}_4^+$	44.86	-4.1	-1.0	5.4	10.9	0.50
$\text{Py}_4^+$	42.95	-3.8	-1.1	7.9	11.3	0.69
$\text{Pyr}_4^+$	46.77	-6.9	-2.1	4.8	6.7	0.71
$\text{N}_{2214}^+$	43.91	-7.4	-1.6	2.2	5.9	0.95
$\text{S}_4^-$	-65.86	1.5	1.5	3.5	9.1	0.39

### 5.3. Roly-poly class

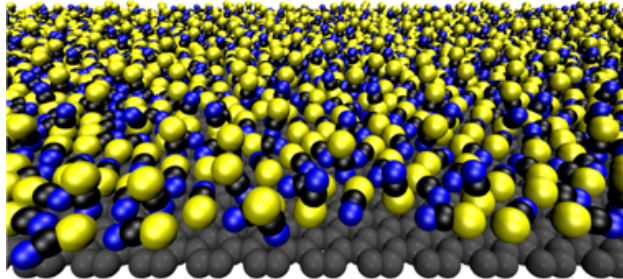
Roly-poly ions, as the class name suggests, can change individual orientation from parallel to perpendicular to the surface with increasing  $|\sigma|$ . Roly-poly ions prefer to lie flat on the surface at low  $|\sigma|$ , but as  $|\sigma|$  to a certain point, ions begin to stand up to make more space for adsorbing ions. [Figure 9](#) shows a particular state where all ions lie parallel to the surface. Increasing  $|\sigma|$  forces ions to stand up increasing the fraction of ions oriented perpendicular to the surface. In the monolayer of roly-poly ions, we observed that both parallel and perpendicular orientations coexist. Moreover, roly-poly can stand up as well as down. In [Figure 9](#), the  $\text{SCN}^-$  ions can contact the surface with both sulphur and nitrogen atoms. In general, roly-poly ions are drastically different from head-tail and ball ions in terms of packing at variable  $|\sigma|$ .

[Table 3](#) summarises simulated and estimated parameters of the modelled ILEIs with roly-poly ions. This data is discussed below.

83 SCN<sup>-</sup> ions (contact layer)



110 SCN<sup>-</sup> ions (monolayer)



128 SCN<sup>-</sup> ions (two layers)

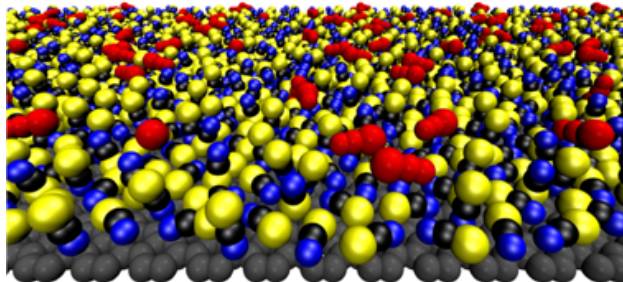


Figure 9: Ball-and-stick model of SCN<sup>-</sup> | electrode interface from the roly-poly ions. First SCN<sup>-</sup> stands when 86 ions are simulated, and the maximum packing density is reached when 110 SCN<sup>-</sup> ions are simulated at the electrode model. Ions of the second layer are shown in red.

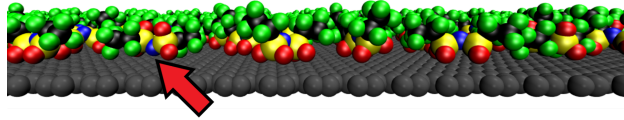
Table 3: Structure-determined parameters of the modelled ILEIs with roly-poly ions.

Ion	$\theta_M [\mu\text{C}\cdot\text{cm}^{-2}]$	$\varphi_M [\text{V}]$	$\varphi_S [\text{V}]$	$C_M [\mu\text{F}\cdot\text{cm}^{-2}]$	$C_S [\mu\text{F}\cdot\text{cm}^{-2}]$	$a$
B(CN) <sub>4</sub> <sup>-</sup>	66.81	11.8	3.1	3.0	5.7	0.96
FSI <sup>-</sup>	58.22	7.0	1.3	2.7	8.3	0.33
C(CN) <sub>3</sub> <sup>-</sup>	73.49	8.3	2.0	4.3	8.9	0.48
N(CN) <sub>2</sub> <sup>-</sup>	110.72	9.4	1.5	3.0	11.8	0.26
SCN <sup>-</sup>	104.99	5.2	0.6	3.6	20.2	0.18

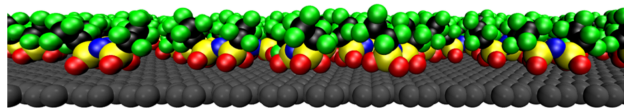
## 5.4. Teeter-totter class

Teeter totter ions are composed of ions which have a binary structure with one central atom connecting two similar groups on both sides.

19 TFSI<sub>2</sub><sup>-</sup> ions (contact layers)



32 TFSI<sub>2</sub><sup>-</sup> ions (monolayers)



34 TFSI<sub>2</sub><sup>-</sup> ions (two layers)

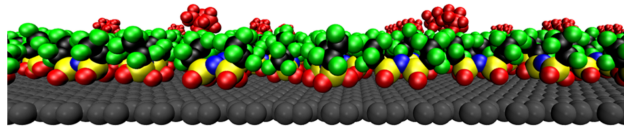


Figure 10: Ball-and-stick model of TFSI<sub>2</sub><sup>-</sup> | electrode interface from the teeter-totter ions. The maximum packing density is reached when 31 TFSI<sub>2</sub><sup>-</sup> ions are simulated at the electrode model. Ions of the second layer are shown in red. One trans-configuration ion is indicated with a red arrow.

Even though the teeter-totter ions can be considered as linear shape and similar to the roly-poly ions, they do not reorient with increasing  $|\sigma|$ . More negatively charged atoms of teeter-totter ions face down the surface at all studied  $|\sigma|$ . Only at very low  $|\sigma|$ , the teeter-totter ions might take a trans-configuration as shown in [Figure 11](#).

[Table 4](#) summarises simulated and estimated parameters of the modelled ILEIs with teeter-totter ions. This data is discussed below.

Table 4: Structure-determined parameters of the modelled ILEIs with teeter-totter ions.

Ion	$\theta_M$ [ $\mu\text{C}\cdot\text{cm}^{-2}$ ]	$\varphi_M$ [V]	$\varphi_S$ [V]	$C_M$ [ $\mu\text{F}\cdot\text{cm}^{-2}$ ]	$C_S$ [ $\mu\text{F}\cdot\text{cm}^{-2}$ ]	$a$
TFSI <sup>-</sup>	-42.00	4.6	1.1	4.6	9.1	0.50
TFSI <sub>2</sub> <sup>-</sup>	-31.50	3.6	0.8	3.9	8.9	0.44

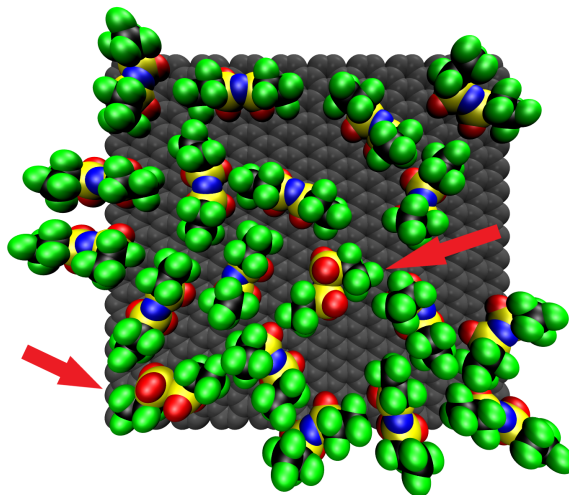


Figure 11: Top view of Ball-and-stick interfacial model of  $\text{TFSl}_2^-$  ions. 15  $\text{TFSl}_2^-$  ions in the system and the arrows indicate trans-configuration ions of a  $\text{TFSl}_2^-$ .

### 5.5. Summary of results

All evaluated  $\Delta\varphi_M - \theta_M$  values along with the curve following Eq. (13) are shown in [Figure 12](#). All data points are given in Tables 1–4 and Appendix Table 2. Judging by the compression factor, it is apparent that most of the ions are ellipses (like  $\text{TFSl}_n^-$  and heads of  $\text{Am}_n^+$  and  $\text{S}_n^-$  with  $k \approx 0.4$ ), some ions are slightly more roundish (halide anions and  $\text{Py}_n^+$  with  $k \approx 0.6$ ), while others are almost roundish (cyano-based anions and  $\text{Pyr}_n^+$  with  $k \approx 0.8$ ). For ball ions, [Figure 12](#) shows an obvious trend of rising  $\Delta\varphi_M$  value with decreasing ion radius. As a clear example, halide ions, which are indicated with purple circles, the smaller the ion, the higher the potential of the monolayer formation. This observation goes *qualitatively* inline with predictions made by Ivaništšev and Fedorov [54], where the maximum packing density was approximated  $\theta_M = q/R^2$ .

For head-tail ions, use radii from Refs. [97–99], Ivaništšev and Fedorov predicted a clear dependence of  $\theta_M$  on the tail length [54]. However, in the presented simulations, only  $\text{Am}_n^+$  shows a clear dependence on the tail length among all simulated head-tail ions. This is probably because the ammonium head and alkyl tail in  $\text{Am}_n^+$  ions have a similar diameter. So tails are touching each other directly. Even though tails do not hold charges, there is van der Waals force and thermal motion that repel tails from each other, so  $\theta_M$  is decreasing with the  $\text{Am}_n^+$  tail lengthening. All  $\text{N}_{2214}^+$ ,  $\text{Im}_n^+$ ,  $\text{Py}_n^+$ , and  $\text{Pyr}_n^+$  have almost the same  $\theta_M$  value, but different  $\Delta\varphi_M$  values due to differences in shape. Their heads are larger in diameter than the alkane tail, so the heads already push tails far from each other, so the tail length can not affect the monolayer density yet does determine the potential drop.

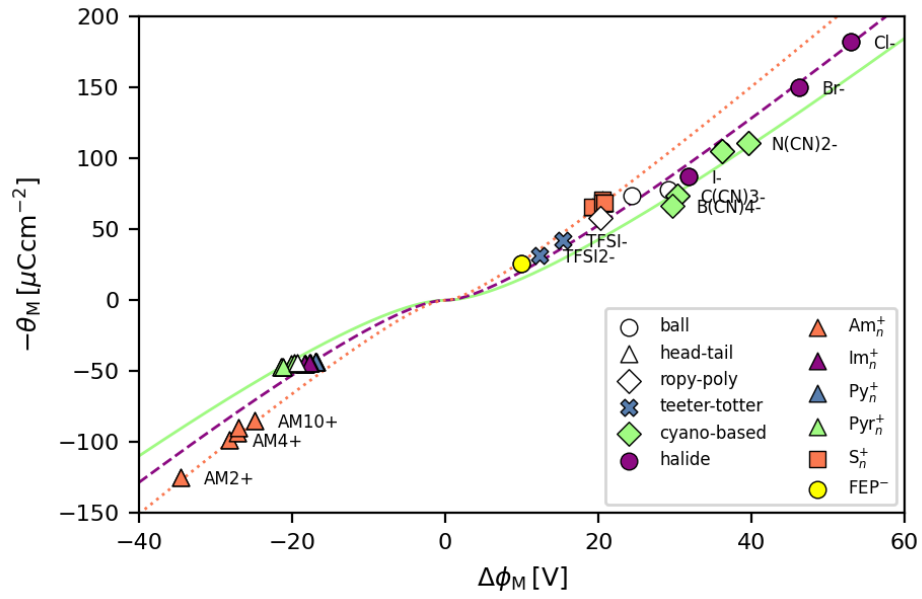


Figure 12: Simulated maximum packing density ( $\theta_M$ ) and monolayer potential drop ( $\Delta\phi_M$ ) values. Lines follow Eq. (13) with  $k$  equals 0.8 (solid), 0.6 (dashed), and 0.4 (dotted).

## 6. DISCUSSIONS

### 6.1. Comparison of structure-determined potentials

Figure 13 summarises all corrected  $\Delta\phi_M - \theta_M$  values. Note that only the  $\Delta\phi_M$  values (obtained with the Poisson equation) are corrected by shifting the surface charge plane by  $-d\theta_M/\epsilon_0$  with  $d = 0.17$  nm and dividing by  $\epsilon_r = 2$ . The shown  $\theta_M$  values correspond to the ion charge  $q = \pm 1e$  as in Figure 12 and all Tables. The most marked feature is that all  $\Delta\phi_M$  values are outside the  $\pm 2$  V vs PZC region – experimentally measurable potential window [59]. In other words, for all studied ions, the true monolayer formation and crowding should not be experimentally reachable. That conclusion holds under the assumption that the partial charge transfer is below  $1 - \sqrt{1/2} = 0.3e$ . The highly polarizable  $\text{Py}_n^+$  could form the monolayer at  $-2$  V upon accepting  $0.5e$  (see Figure 13) and halide anions could form their monolayers at  $+2$  V upon donating  $0.7e$ . The scanning tunnelling microscopy study of  $\text{Py}_4^+$  adsorption from  $\text{Py}_4\text{BF}_4$  did not reveal any ordered structure [100]. On the opposite, halide anions are well known for forming highly ordered adlayers even at lower relative potentials [101,102]. Thus, it is worth examining whether these adlayers meet the monolayer definition by checking for evidence of overscreening and crowding.

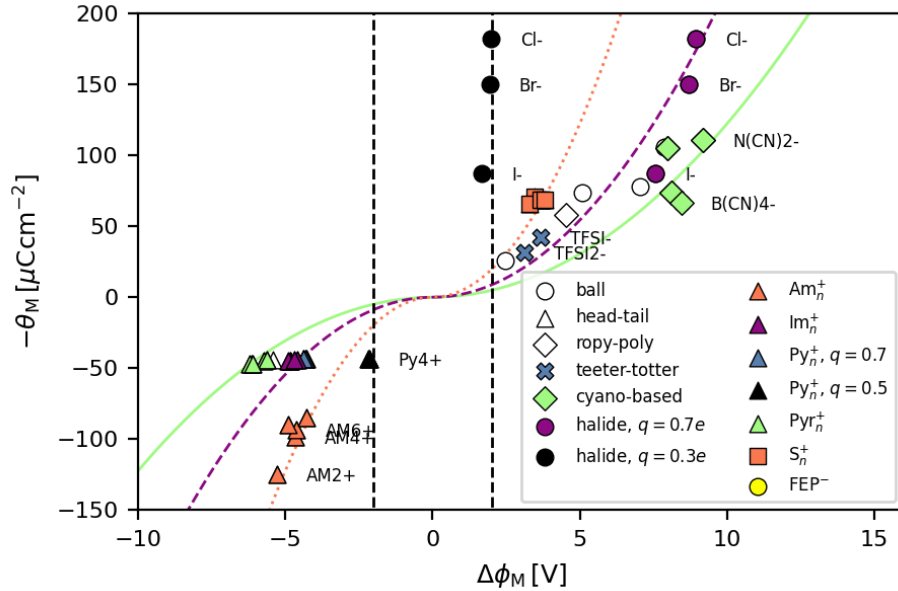


Figure 13: Simulated maximum packing density ( $\theta_M$ ) and recalculated monolayer potential drop ( $\Delta\phi_M$ ) values. Lines follow Eq. (13) with  $d = 0$ ,  $\epsilon_r = 2$ , and  $k$  equals 0.8 (solid), 0.6 (dashed), and 0.4 (dotted).

The most important finding of this work is that estimated  $\Delta\phi_s$  values are within the  $\pm 2$  V region as can be seen in Tables 1–4. We suggest that most of the reported ordered adlayers [16,18,22,37,39,103–107] form in the vicinity of the saturation potential ( $\Delta\phi_s$ ). That conclusion is supported by the results of two electrode simulations of BMImPF<sub>6</sub> [56], where  $\Delta\phi_s$  of 3 V was estimated for PF<sub>6</sub><sup>−</sup> anions. In this work, the corresponding estimation is 2.2 V with  $\epsilon_r = 1.6$  as in the referred MD simulations. Despite crude approximations in Eq. (11) for  $\Delta\phi_s$ , it leads to a phenomenologically reasonable conclusion that previously reported ILEI processes are most probably happening in the overscreening regime, *i. e.*, far from crowding.

## 6.2. Ion shape and the monolayer potential

Let us use the obtained data to answer an essential question – whether monolayers of physisorbed ions are in principle achievable. The criteria for such a possibility is a realistically low  $|\Delta\phi_M|$  value below 2 V. For the ball ions, the potential can be translated into a radius of over 1.13 nm assuming that  $\epsilon_r = 2$  and  $d = 0$  in Eq. (13). In other words, hard ball ions of  $\mp 1e$  charge and 1.13 nm radius form a monolayer at  $\pm 2$  V. All studied and most known ILs ions have much smaller dimensions. Let us take for example a polyoxometalate PW<sub>12</sub>O<sub>40</sub><sup>3−</sup> anions that was used by Borukhov *et al.* in Refs. [108,109] to illustrate the idea of crowding. PW<sub>12</sub>O<sub>40</sub><sup>3−</sup> has a radius of 0.55 nm and an ion charge of  $-3e$ . A simple estimation of  $\Delta\phi_M$  for PW<sub>12</sub>O<sub>40</sub><sup>3−</sup> gives an unreachable potential value of +12 V!

Figure 13 hints at the way of lowering the  $\Delta\phi_M$  by decreasing the compression factor. Indeed a flat “pancake” cation with  $r = 0.17$  nm and  $R = 0.44$  nm ( $k \approx 0.4$ ) should form a monolayer at  $-2$  V. That is comparable to the size of 3N-coronene cations – one of the smallest representatives of nitrogen-substituted polycyclic aromatic hydrocarbon (PAH) cations [110]. Similar PAH could be substituted with boron [111] to give pancake anions. To the best of our knowledge, such PAH-based ILs are unknown. Herewith, boron or nitrogen doped PAH anions and cations are potential candidates for crowding at relatively small potentials. Experimental and computational study of such ions promises the discovery of exciting new phenomena.

## 6.3. Concluding remarks and future research directions

By comparing the estimated  $\Delta\phi_M$  and  $\Delta\phi_s$  values to empirical data, we conclude that the monolayer and crowded structures of studied ions are unreachable within experimentally measurable potential windows. Our data along with the classification of ions suggest

designing “pancake” ions that can form crowded structures. Reaching the crowded regime can reveal new phenomena of high application potential as predicted and discussed in Ref. [112]. For the common ions, we conclude that previously observed adlayers of such ions are formed in the vicinity of  $\Delta\phi_S$ , *i. e.*, in the overscreening regime. It is also essential to understand the nature of these adlayers at ILEI from both fundamental and application perspectives.

On top of that, the data generated in this work includes estimations for capacitances ( $C_M$  and  $C_S$ ) as well as geometric parameters ( $l$  and  $\delta$ ) which can be utilised in supercapacitors, electric actuators and sensors research. Our workflow can be updated to insert co-ions into the models and run more realistic MD simulations. Moreover, due to the small size of such models (even with co-ions), they are suitable for DFT calculations of more realistic potential drops. Overall, the presented work forms the ground for further research in multiple directions with fascinating perspectives.

## 7. SUMMARY

In this study, we have tried out an original workflow of ionic liquid–electrode interface (ILEI) simulations. Our one electrode ILEI model is suitable for describing the monolayer and crowded structures at a computational cost two orders of magnitude lower than the two electrode models. We have tested the workflow on 40 ions using molecular dynamics simulations and obtained maximum packing densities ( $\theta_M$ ) of these layers packed in monolayers – a state at which a single layer of ions completely screens the surface charge density ( $\sigma$ ). By examining structural changes under variable  $\sigma$  we have classified all studied ions into balls, roly-poly, teeter-totter, and head-tail classes. Using the simulated  $\theta_M$  values we estimated structure-determined ILEI properties: potential drop across the monolayer ( $\Delta\phi_M$ ), corresponding capacitance ( $C_M$ ), the potential drop across the saturated ILEI ( $\Delta\phi_S$ ), and corresponding capacitance ( $C_S$ ). Based on the comparison of  $\Delta\phi_M$  and  $\Delta\phi_S$  with empirical data, we conclude that for the studied ions the monolayer formation is impossible within the measurable potential window and that experimentally observed structures are probably forming close to the saturation state.

## 8. REFERENCES

- [1] G. Velpula, R. Phillipson, J.X. Lian, D. Cornil, P. Walke, K. Verguts, et al., Graphene Meets Ionic Liquids: Fermi Level Engineering via Electrostatic Forces, *ACS Nano*. 13 (2019) 3512–3521.
- [2] S. Xu, S. Xing, S.-S. Pei, V. Ivaništšev, R. Lynden-Bell, S. Baldelli, Molecular Response of 1-Butyl-3-Methylimidazolium Dicyanamide Ionic Liquid at the Graphene Electrode Interface Investigated by Sum Frequency Generation Spectroscopy and Molecular Dynamics Simulations, *J. Phys. Chem. C*. 119 (2015) 26009–26019.
- [3] A.B. Biedron, E.L. Garfunkel, E.W. Castner, S. Rangan, Ionic liquid ultrathin films at the surface of Cu(100) and Au(111), *J. Chem. Phys.* 146 (2017) 054704.
- [4] M. Chu, M. Miller, T. Douglas, P. Dutta, Ultraslow Dynamics at a Charged Silicon–Ionic Liquid Interface Revealed by X-ray Reflectivity, *J. Phys. Chem. C*. 121 (2017) 3841–3845.
- [5] R. Yamamoto, H. Morisaki, O. Sakata, H. Shimotani, H. Yuan, Y. Iwasa, et al., External electric field dependence of the structure of the electric double layer at an ionic liquid/Au interface, *Appl. Phys. Lett.* 101 (2012) 053122.
- [6] N. Nishi, T. Uruga, H. Tanida, T. Kakiuchi, Temperature Dependence of Multilayering at the Free Surface of Ionic Liquids Probed by X-ray Reflectivity Measurements, *Langmuir*. 27 (2011) 7531–7536.
- [7] P. Reichert, K.S. Kjær, T.B. van Driel, J. Mars, J.W. Ochsman, D. Pontoni, et al., Molecular scale structure and dynamics at an ionic liquid/electrode interface, *Faraday Discuss.* 206 (2017) 141–157.
- [8] M. Mezger, R. Roth, H. Schröder, P. Reichert, D. Pontoni, H. Reichert, Solid-liquid interfaces of ionic liquid solutions—Interfacial layering and bulk correlations, *J. Chem. Phys.* 142 (2015) 164707.
- [9] T.A. Petach, A. Mehta, R. Marks, B. Johnson, M.F. Toney, D. Goldhaber-Gordon, Voltage-Controlled Interfacial Layering in an Ionic Liquid on SrTiO<sub>3</sub>, *ACS Nano*. 10 (2016) 4565–4569.
- [10] M. Chu, M. Miller, P. Dutta, Crowding and Anomalous Capacitance at an Electrode–Ionic Liquid Interface Observed Using Operando X-ray Scattering, *ACS Cent. Sci.* 2 (2016) 175–180.
- [11] N. Nishi, J. Uchiyashiki, Y. Ikeda, S. Katakura, T. Oda, M. Hino, et al., Potential-Dependent Structure of the Ionic Layer at the Electrode Interface of an Ionic Liquid Probed Using Neutron Reflectometry, *J. Phys. Chem. C*. 123 (2019) 9223–9230.
- [12] S. Katakura, K. Amano, T. Sakka, W. Bu, B. Lin, M.L. Schlossman, et al., Evolution and Reversible Polarity of Multilayering at the Ionic Liquid/Water Interface, *J. Phys. Chem. B*. 124 (2020) 6412–6419.
- [13] S. Katakura, N. Nishi, K. Kobayashi, K. Amano, T. Sakka, Effect of Switching the Length of Alkyl Chains on Electric Double Layer Structure and Differential Capacitance at the Electrode Interface of Quaternary Ammonium-Based Ionic Liquids Studied Using Molecular Dynamics Simulation, *J. Phys. Chem. C*. 124 (2020) 7873–7883.
- [14] S. Zhang, T. Sakka, N. Nishi, Slow and Fast Dynamics at the Ionic Liquid/Gold Electrode Interface Separately Probed by Electrochemical Surface Plasmon Resonance Combined with Sequential Potential Pulse Techniques, *J. Electrochem. Soc.* (2022).
- [15] A. Uysal, H. Zhou, G. Feng, S.S. Lee, S. Li, P.T. Cummings, et al., Interfacial ionic ‘liquids’: connecting static and dynamic structures, *J. Phys. Condens. Matter*. 27 (2015) 032101.
- [16] Y.-Z. Su, J.-W. Yan, M.-G. Li, Z.-X. Xie, B.-W. Mao, Z.-Q. Tian, Adsorption of

- Solvent Cations on Au(111) and Au(100) in Alkylimidazolium-Based Ionic Liquids - Worm-Like versus Micelle-Like Structures, *Z. Phys. Chem.-Int. J. Res.* 226 (2012) 979–994.
- [17] A.J. Page, A. Elbourne, R. Stefanovic, M.A. Addicoat, G.G. Warr, K. Voïtchovsky, et al., 3-Dimensional atomic scale structure of the ionic liquid–graphite interface elucidated by AM-AFM and quantum chemical simulations, *Nanoscale*. 6 (2014) 8100–8106.
- [18] N. Borisenko, S.Z. El Abedin, F. Endres, An in Situ STM and DTS Study of the Extremely Pure [EMIM]FAP/Au(111) Interface, *Chemphyschem*. 13 (2012) 1736–1742.
- [19] F. Buchner, K. Forster-Tonigold, B. Uhl, D. Alwast, N. Wagner, A. Groß, et al., Towards the Microscopic Identification of Anions and Cations at the Ionic Liquid | Ag(111) Interface: A Combined Experimental and Theoretical Investigation, *ACS Nano*. 7 (2013) 7773–7784.
- [20] J. Hoth, F. Hausen, M.H. Müser, R. Bennewitz, Force microscopy of layering and friction in an ionic liquid, *J. Phys. Condens. Matter*. 26 (2014) 284110.
- [21] J.M. Black, D. Walters, A. Labuda, G. Feng, P.C. Hillesheim, S. Dai, et al., Bias-Dependent Molecular-Level Structure of Electrical Double Layer in Ionic Liquid on Graphite, *Nano Lett.* 13 (2013) 5954–5960.
- [22] R. Atkin, N. Borisenko, M. Drüschler, S.Z. El Abedin, F. Endres, R. Hayes, et al., An in situ STM/AFM and impedance spectroscopy study of the extremely pure 1-butyl-1-methylpyrrolidinium tris(pentafluoroethyl)trifluorophosphate/Au(111) interface: potential dependent solvation layers and the herringbone reconstruction, *Phys. Chem. Chem. Phys.* 13 (2011) 6849–6857.
- [23] X. Gong, A. Kozbial, F. Rose, L. Li, Effect of  $\pi$ - $\pi^+$  Stacking on the Layering of Ionic Liquids Confined to an Amorphous Carbon Surface, *ACS Appl. Mater. Interfaces*. 7 (2015) 7078–7081.
- [24] X. Gong, A. Kozbial, L. Li, What causes extended layering of ionic liquids on the mica surface?, *Chem. Sci.* 6 (2015) 3478–3482.
- [25] A. Elbourne, S. McDonald, K. Voïchovsky, F. Endres, G.G. Warr, R. Atkin, Nanostructure of the Ionic Liquid–Graphite Stern Layer, *ACS Nano*. 9 (2015) 7608–7620.
- [26] L.A. Jurado, R.M. Espinosa-Marzal, Insight into the Electrical Double Layer of an Ionic Liquid on Graphene, *Sci. Rep.* 7 (2017) 4225.
- [27] M.-G. Li, L. Chen, Y.-X. Zhong, Z.-B. Chen, J.-W. Yan, B.-W. Mao, The electrochemical interface of Ag(111) in 1-ethyl-3-methylimidazolium bis(trifluoromethylsulfonyl)imide ionic liquid—A combined in-situ scanning probe microscopy and impedance study, *Electrochimica Acta*. 197 (2016) 282–289.
- [28] N. Hjalmarsson, R. Atkin, M.W. Rutland, Is the boundary layer of an ionic liquid equally lubricating at higher temperature?, *Phys. Chem. Chem. Phys.* 18 (2016) 9232–9239.
- [29] V. Lockett, M. Horne, R. Sedev, T. Rodopoulos, J. Ralston, Differential capacitance of the double layer at the electrode/ionic liquids interface, *Phys. Chem. Chem. Phys.* 12 (2010) 12499–12512.
- [30] M. Gnahn, C. Berger, M. Arkhipova, H. Kunkel, T. Pajkossy, G. Maas, et al., The interfaces of Au(111) and Au(100) in a hexaalkyl-substituted guanidinium ionic liquid: an electrochemical and in situ STM study, *Phys. Chem. Chem. Phys.* 14 (2012) 10647–10652.
- [31] M. Gnahn, C. Müller, R. Répánszki, T. Pajkossy, D.M. Kolb, The interface between Au(100) and 1-butyl-3-methyl-imidazolium-hexafluorophosphate, *Phys. Chem. Chem.*

- Phys. 13 (2011) 11627–11633.
- [32] J. Wallauer, M. Drüschler, B. Huber, B. Roling, The Differential Capacitance of Ionic Liquid | Metal Electrode Interfaces – A Critical Comparison of Experimental Results with Theoretical Predictions, *Z. Für Naturforschung B.* 68b (2013) 1143–1153.
- [33] Y. Su, J. Yan, M. Li, M. Zhang, B. Mao, Electric Double Layer of Au(100)/Imidazolium-Based Ionic Liquids Interface: Effect of Cation Size, *J. Phys. Chem. C.* 117 (2013) 205–212.
- [34] C. Gomes, R. Costa, C.M. Pereira, A.F. Silva, The electrical double layer at the ionic liquid/Au and Pt electrode interface, *RSC Adv.* 4 (2014) 28914–28921.
- [35] R. Costa, I.V. Voroshylova, M.N.D.S. Cordeiro, C.M. Pereira, A.F. Silva, Enhancement of differential double layer capacitance and charge accumulation by tuning the composition of ionic liquids mixtures, *Electrochimica Acta.* 261 (2018) 214–220.
- [36] N. Zhang, X.-R. Wang, Y.-X. Yuan, H.-F. Wang, M.-M. Xu, Z.-G. Ren, et al., Probing double layer structure at Au/[BMIm]BF<sub>4</sub> interface by molecular length-dependent SERS Stark effect, *J. Electroanal. Chem.* 751 (2015) 137–143.
- [37] G.-B. Pan, W. Freyland, 2D phase transition of PF<sub>6</sub> adlayers at the electrified ionic liquid/Au(111) interface, *Chem. Phys. Lett.* 427 (2006) 96–100.
- [38] Y.-Z. Su, Y.-C. Fu, J.-W. Yan, Z.-B. Chen, B.-W. Mao, Double Layer of Au(100)/Ionic Liquid Interface and Its Stability in Imidazolium-Based Ionic Liquids, *Angew. Chem. Int. Ed.* 48 (2009) 5148–5151.
- [39] T. Pajkossy, C. Müller, T. Jacob, The metal–ionic liquid interface as characterized by impedance spectroscopy and in situ scanning tunneling microscopy, *Phys. Chem. Chem. Phys.* 20 (2018) 21241–21250.
- [40] J.M. Klein, H. Squire, B. Gurkan, Electroanalytical Investigation of the Electrode–Electrolyte Interface of Quaternary Ammonium Ionic Liquids: Impact of Alkyl Chain Length and Ether Functionality, *J. Phys. Chem. C.* 124 (2020) 5613–5623.
- [41] W. Dean, J. Klein, B. Gurkan, Do Deep Eutectic Solvents Behave Like Ionic Liquid Electrolytes? A Perspective from the Electrode-Electrolyte Interface, *J. Electrochem. Soc.* 168 (2021) 026503.
- [42] M. Belotti, X. Lyu, L. Xu, P. Halat, N. Darwish, D.S. Silvester, et al., Experimental Evidence of Long-Lived Electric Fields of Ionic Liquid Bilayers, *J. Am. Chem. Soc.* 143 (2021) 17431–17440.
- [43] N. Hjalmarsson, D. Wallinder, S. Glavatskih, R. Atkin, T. Aastrup, M.W. Rutland, Weighing the surface charge of an ionic liquid, *Nanoscale.* 7 (2015) 16039–16045.
- [44] M. Schammer, A. Latz, B. Horstmann, The Role of Energy Scales for the Structure of Ionic Liquids at Electrified Interfaces: A Theory-Based Approach, *J. Phys. Chem. B.* 126 (2022) 2761–2776.
- [45] M.Z. Bazant, B.D. Storey, A.A. Kornyshev, Double Layer in Ionic Liquids: Overscreening versus Crowding, *Phys. Rev. Lett.* 106 (2011) 046102.
- [46] J.P. de Souza, Z.A.H. Goodwin, M. McEldrew, A.A. Kornyshev, M.Z. Bazant, Interfacial Layering in the Electric Double Layer of Ionic Liquids, *Phys. Rev. Lett.* 125 (2020) 116001.
- [47] N. Gavish, A. Yochelis, Theory of Phase Separation and Polarization for Pure Ionic Liquids, *J. Phys. Chem. Lett.* 7 (2016) 1121–1126.
- [48] M.V. Fedorov, A.A. Kornyshev, Towards understanding the structure and capacitance of electrical double layer in ionic liquids, *Electrochimica Acta.* 53 (2008) 6835–6840.
- [49] M.V. Fedorov, A.A. Kornyshev, Ionic Liquid Near a Charged Wall: Structure and Capacitance of Electrical Double Layer, *J. Phys. Chem. B.* 112 (2008) 11868–11872.
- [50] M. Giroto, A.M. Alencar, Modified 3D Ewald Summation for Slab Geometry at Constant Potential, *J. Phys. Chem. B.* 124 (2020) 7842–7848.

- [51] K. Kirchner, T. Kirchner, V. Ivaništšev, M.V. Fedorov, Electrical double layer in ionic liquids: Structural transitions from multilayer to monolayer structure at the interface, *Electrochimica Acta*. 110 (2013) 762–771.
- [52] J.L. Ma, Q. Meng, J. Fan, Charge driven lateral structural evolution of ions in electric double layer capacitors strongly correlates with differential capacitance, *Phys. Chem. Chem. Phys.* 20 (2018) 8054–8063.
- [53] S. Begić, F. Chen, E. Jónsson, M. Forsyth, Overscreening and crowding in electrochemical ionic liquid systems, *Phys. Rev. Mater.* 3 (2019) 095801.
- [54] V. Ivaništšev, M.V. Fedorov, Interfaces between Charged Surfaces and Ionic Liquids: Insights from Molecular Simulations, *Electrochem. Soc. Interface*. 23 (2014) 65–69.
- [55] V. Ivaništšev, S. O’Connor, M.V. Fedorov, Poly(a)morphic portrait of the electrical double layer in ionic liquids, *Electrochem. Commun.* 48 (2014) 61–64.
- [56] I.V. Voroshylova, H. Ers, V. Koverga, B. Docampo-Álvarez, P. Pikma, V.B. Ivaništšev, et al., Ionic liquid–metal interface: The origins of capacitance peaks, *Electrochimica Acta*. 379 (2021) 138148.
- [57] N. Georgi, A.A. Kornyshev, M.V. Fedorov, The anatomy of the double layer and capacitance in ionic liquids with anisotropic ions: Electrostriction vs. lattice saturation, *J. Electroanal. Chem.* 649 (2010) 261–267.
- [58] S. Sharma, H.K. Kashyap, Structure of Quaternary Ammonium Ionic Liquids at Interfaces: Effects of Cation Tail Modification with Isoelectronic Groups, *J. Phys. Chem. C*. 119 (2015) 23955–23967.
- [59] S.A. Kislenko, Yu.O. Moroz, K. Karu, V.B. Ivaništšev, M.V. Fedorov, Calculating the Maximum Density of the Surface Packing of Ions in Ionic Liquids, *Russ. J. Phys. Chem. A*. 92 (2018) 999–1005.
- [60] A.A. Kornyshev, E. Spohr, M.A. Vorotyntsev, Electrochemical Interfaces: At the Border Line, in: A. J. Bard, M. Stratmann, E. Gileadi, M. Urbakh (Eds.), *Encycl. Electrochem. Thermodyn. Electrified Interfaces*, Wiley VCH, Weinheim, 2002: pp. 33–132.
- [61] G. Gouy, Sur la constitution de la charge électrique à la surface d’un électrolyte, *J Phys Theor Appl*. 9 (1910) 457–458.
- [62] A.A. Kornyshev, Double-Layer in Ionic Liquids: Paradigm Change?, *J. Phys. Chem. B*. 111 (2007) 5545–5557.
- [63] Z.A.H. Goodwin, G. Feng, A.A. Kornyshev, Mean-Field Theory of Electrical Double Layer In Ionic Liquids with Account of Short-Range Correlations, *Electrochimica Acta*. 225 (2017) 190–197.
- [64] O. Stern, Zur theorie der elektrolytischen doppelschicht, *Z. Für Elektrochem. Angew. Phys. Chem.* 30 (1924) 508–516.
- [65] I.V. Voroshylova, H. Ers, B. Docampo-Álvarez, P. Pikma, V.B. Ivaništšev, M.N.D.S. Cordeiro, Hysteresis in the MD Simulations of Differential Capacitance at the Ionic Liquid–Au Interface, *J. Phys. Chem. Lett.* 11 (2020) 10408–10413.
- [66] V. Ivaništšev, K. Kirchner, T. Kirchner, M.V. Fedorov, Restructuring of the electrical double layer in ionic liquids upon charging, *J. Phys. Condens. Matter*. 27 (2015) 102101.
- [67] H. Ers, I.V. Voroshylova, P. Pikma, V. Ivanistsev, Double layer in ionic liquids: temperature effect and bilayer model, *J. Mol. Liq.* (2022).
- [68] K.B. Oldham, A Gouy-Chapman-Stern model of the double layer at a metal/ionic liquid interface, *J. Electroanal. Chem.* 613 (2008) 131–138.
- [69] M.S. Kilic, M.Z. Bazant, A. Ajdari, Steric effects in the dynamics of electrolytes at large applied voltages. I. Double-layer charging, *Phys. Rev. E*. 75 (2007) 021502.
- [70] M.S. Kilic, M.Z. Bazant, A. Ajdari, Steric effects in the dynamics of electrolytes at

- large applied voltages. II. Modified Poisson-Nernst-Planck equations, *Phys. Rev. E*. 75 (2007) 021503.
- [71] R.M. Lynden-Bell, M.G. Del Pópolo, T.G.A. Youngs, J. Kohanoff, C.G. Hanke, J.B. Harper, et al., Simulations of Ionic Liquids, Solutions, and Surfaces, *Acc. Chem. Res.* 40 (2007) 1138–1145.
- [72] A.H. Larsen, J.J. Mortensen, J. Blomqvist, I.E. Castelli, R. Christensen, M. Dulak, et al., The atomic simulation environment—a Python library for working with atoms, *J. Phys. Condens. Matter*. 29 (2017) 273002.
- [73] L. Martínez, R. Andrade, E.G. Birgin, J.M. Martínez, PACKMOL: A Package for Building Initial Configurations for Molecular Dynamics Simulations, *J. Comput. Chem.* 30 (2009) 2157–2164.
- [74] M.J. Abraham, T. Murtola, R. Schulz, S. Páll, J.C. Smith, B. Hess, et al., GROMACS: High performance molecular simulations through multi-level parallelism from laptops to supercomputers, *SoftwareX*. 1–2 (2015) 19–25.
- [75] S. Pronk, S. Páll, R. Schulz, P. Larsson, P. Bjelkmar, R. Apostolov, et al., GROMACS 4.5: a high-throughput and highly parallel open source molecular simulation toolkit, *Bioinformatics*. 29 (2013) 845–854.
- [76] B. Hess, C. Kutzner, D. Van Der Spoel, E. Lindahl, GROMACS 4: algorithms for highly efficient, load-balanced, and scalable molecular simulation, *J. Chem. Theory Comput.* 4 (2008) 435–447.
- [77] D. Van Der Spoel, E. Lindahl, B. Hess, G. Groenhof, A.E. Mark, H.J.C. Berendsen, GROMACS: Fast, flexible, and free, *J. Comput. Chem.* 26 (2005) 1701–1718.
- [78] S. Páll, M.J. Abraham, C. Kutzner, B. Hess, E. Lindahl, Tackling Exascale Software Challenges in Molecular Dynamics Simulations with GROMACS, in: S. Markidis, E. Laure (Eds.), *Solving Softw. Chall. Exascale*, Springer International Publishing, Cham, 2015: pp. 3–27.
- [79] E. Lindahl, B. Hess, D. van der Spoel, GROMACS 3.0: a package for molecular simulation and trajectory analysis, *Mol. Model. Annu.* 7 (2001) 306–317.
- [80] H.J.C. Berendsen, D. van der Spoel, R. van Drunen, GROMACS: A message-passing parallel molecular dynamics implementation, *Comput. Phys. Commun.* 91 (1995) 43–56.
- [81] U. Essmann, L. Perera, M.L. Berkowitz, T. Darden, H. Lee, L.G. Pedersen, A smooth particle mesh Ewald method, *J. Chem. Phys.* 103 (1995) 8577–8593.
- [82] I.-C. Yeh, M.L. Berkowitz, Ewald summation for systems with slab geometry, *J. Chem. Phys.* 111 (1999) 3155–3162.
- [83] G. Bussi, D. Donadio, M. Parrinello, Canonical sampling through velocity rescaling, *J. Chem. Phys.* 126 (2007) 014101.
- [84] N. Michaud-Agrawal, E.J. Denning, T.B. Woolf, O. Beckstein, MDAnalysis: a toolkit for the analysis of molecular dynamics simulations, *J. Comput. Chem.* 32 (2011) 2319–2327.
- [85] R.J. Gowers, M. Linke, J. Barnoud, T.J.E. Reddy, M.N. Melo, S.L. Seyler, et al., MDAnalysis: a Python package for the rapid analysis of molecular dynamics simulations, Los Alamos National Lab.(LANL), Los Alamos, NM (United States), 2019.
- [86] W. Humphrey, A. Dalke, K. Schulten, VMD: Visual molecular dynamics, *J. Mol. Graph.* 14 (1996) 33–38.
- [87] E. Roos Nerut, K. Karu, I.V. Voroshylova, K. Kirchner, T. Kirchner, M.V. Fedorov, et al., NaRIBaS—A Scripting Framework for Computational Modeling of Nanomaterials and Room Temperature Ionic Liquids in Bulk and Slab, *Computation*. 6 (2018) 57.
- [88] C. Schröder, Comparing reduced partial charge models with polarizable simulations of

- ionic liquids, *Phys. Chem. Chem. Phys.* 14 (2012) 3089–3102.
- [89] I.V. Voroshylova, M. Lembinen, H. Ers, M. Mišin, V.A. Koverga, C.M. Pereira, et al., On the role of the surface charge plane position at Au(hkl)–BMImPF6 interfaces, *Electrochimica Acta.* 318 (2019) 76–82.
- [90] N.D. Lang, W. Kohn, Theory of Metal Surfaces: Induced Surface Charge and Image Potential, *Phys. Rev. B.* 7 (1973) 3541–3550.
- [91] N.D. Lang, W. Kohn, Theory of Metal Surfaces: Work Function, *Phys. Rev. B.* 3 (1971) 1215–1223.
- [92] N.B. Luque, W. Schmickler, The electric double layer on graphite, *Electrochimica Acta.* 71 (2012) 82–85.
- [93] A.A. Kornyshev, N.B. Luque, W. Schmickler, Differential capacitance of ionic liquid interface with graphite: the story of two double layers, *J. Solid State Electrochem.* 18 (2014) 1345–1349.
- [94] O.M. Magnussen, Ordered Anion Adlayers on Metal Electrode Surfaces, *Chem. Rev.* 102 (2002) 679–726.
- [95] C. Noh, Y. Jung, Understanding the charging dynamics of an ionic liquid electric double layer capacitor via molecular dynamics simulations, *Phys. Chem. Chem. Phys.* 21 (2019) 6790–6800.
- [96] F. Tang, T. Ohto, T. Hasegawa, M. Bonn, Y. Nagata,  $\pi^+-\pi^+$  stacking of imidazolium cations enhances molecular layering of room temperature ionic liquids at their interfaces, *Phys Chem Chem Phys.* 19 (2017) 2850–2856.
- [97] A.J.L. Costa, M.R.C. Soromenho, K. Shimizu, I.M. Marrucho, J.M.S.S. Esperança, J.N.C. Lopes, et al., Density, Thermal Expansion and Viscosity of Cholinium-Derived Ionic Liquids, *ChemPhysChem.* 13 (2012) 1902–1909.
- [98] M. Součková, J. Klomfar, J. Pátek, Surface tension and 0.1 MPa densities of imidazolium-, pyridinium-, pyrrolidinium-, and piperidinium-based tris(pentafluoroethyl)trifluorophosphate ionic liquids, *Fluid Phase Equilibria.* 333 (2012) 38–46.
- [99] W.M. Haynes, D.R. Lide, T.J. Bruno, *CRC handbook of chemistry and physics*, CRC press Boca Raton, FL, 2017.
- [100] E. Anderson, V. Grozovski, L. Siinor, C. Siimenson, V. Ivaništšev, K. Lust, et al., Influence of the electrode potential and in situ STM scanning conditions on the phase boundary structure of the single crystal Bi(1 1 1)|1-butyl-4-methylpyridinium tetrafluoroborate interface, *J. Electroanal. Chem.* 709 (2013) 46–56.
- [101] O. Oll, M. Väärtnõu, G. Gorbatovski, J. Zhao, C. Siimenson, L. Siinor, et al., Adsorption of anions on bismuth and cadmium single crystal plane electrodes from various solvents and ionic liquid mixtures, *Electrochimica Acta.* 319 (2019) 895–908.
- [102] O. Oll, C. Siimenson, K. Lust, G. Gorbatovski, E. Lust, Specific adsorption from an ionic liquid: impedance study of iodide ion adsorption from a pure halide ionic liquid at bismuth single crystal planes, *Electrochimica Acta.* 247 (2017) 910–919.
- [103] X. Zhang, Y.-X. Zhong, J.-W. Yan, Y.-Z. Su, M. Zhang, B.-W. Mao, Probing double layer structures of Au (111)–BMIPF 6 ionic liquid interfaces from potential-dependent AFM force curves, *Chem. Commun.* 48 (2012) 582–584.
- [104] E. Anderson, V. Grozovski, L. Siinor, C. Siimenson, E. Lust, In situ STM studies of Bi(111)|1-ethyl-3-methylimidazolium tetrafluoroborate + 1-ethyl-3-methylimidazolium iodide interface, *Electrochem. Commun.* 46 (2014) 18–21.
- [105] R. Wen, B. Rahn, O.M. Magnussen, Potential-Dependent Adlayer Structure and Dynamics at the Ionic Liquid/Au(111) Interface: A Molecular-Scale In Situ Video-STM Study, *Angew. Chem. Int. Ed.* 54 (2015) 6062–6066.
- [106] R. Wen, B. Rahn, Olaf.M. Magnussen, In Situ Video-STM Study of Adlayer Structure

- and Surface Dynamics at the Ionic Liquid/Au (111) Interface, *J. Phys. Chem. C*. 120 (2016) 15765–15771.
- [107] Y. Fu, A.V. Rudnev, Scanning probe microscopy of an electrode/ionic liquid interface, *Curr. Opin. Electrochem.* 1 (2017) 59–65.
- [108] I. Borukhov, D. Andelman, H. Orland, Adsorption of large ions from an electrolyte solution: a modified Poisson–Boltzmann equation, *Electrochimica Acta*. 46 (2000) 221–229.
- [109] I. Borukhov, D. Andelman, H. Orland, Steric Effects in Electrolytes: A Modified Poisson-Boltzmann Equation, *Phys. Rev. Lett.* 79 (1997) 435–438.
- [110] D.M. Hudgins, Jr. Charles W. Bauschlicher, L.J. Allamandola, Variations in the Peak Position of the 6.2  $\mu\text{m}$  Interstellar Emission Feature: A Tracer of N in the Interstellar Polycyclic Aromatic Hydrocarbon Population, *Astrophys. J.* 632 (2005) 316–332.
- [111] L.-F. Velázquez-López, S.-M. Pacheco-Ortín, R. Mejía-Olvera, E. Agacino-Valdés, DFT study of CO adsorption on nitrogen/boron doped-graphene for sensor applications, *J. Mol. Model.* 25 (2019) 91.
- [112] M.Z. Bazant, M.S. Kilic, B.D. Storey, A. Ajdari, Towards an understanding of induced-charge electrokinetics at large applied voltages in concentrated solutions, *Adv. Colloid Interface Sci.* 152 (2009) 48–88.

## 9. APPENDICES

9.1. Table 1. Nomenclature names and acronyms of all simulated ions

ion name	acronym
<b>Head-tail class</b>	
ethylammonium	Am <sub>2</sub> <sup>+</sup>
butylammonium	Am <sub>4</sub> <sup>+</sup>
hexylammonium	Am <sub>6</sub> <sup>+</sup>
octylammonium	Am <sub>8</sub> <sup>+</sup>
decylammonium	Am <sub>10</sub> <sup>+</sup>
1-ethyl-3-methylimidazolium	Im <sub>2</sub> <sup>+</sup>
1-butyl-3-methylimidazolium	Im <sub>4</sub> <sup>+</sup>
1-hexyl-3-methylimidazolium	Im <sub>6</sub> <sup>+</sup>
1-octyl-3-methylimidazolium	Im <sub>8</sub> <sup>+</sup>
1-decyl-3-methylimidazolium	Im <sub>10</sub> <sup>+</sup>
butyldiethylmethylammonium	N <sub>2214</sub> <sup>+</sup>
1-ethyl-1-methylpyridinium	Py <sub>2</sub> <sup>+</sup>
1-butyl-1-methylpyridinium	Py <sub>4</sub> <sup>+</sup>
1-hexyl-1-methylpyridinium	Py <sub>6</sub> <sup>+</sup>
1-methyl-1-octylpyridinium	Py <sub>8</sub> <sup>+</sup>
1-decyl-1-methylpyridinium	Py <sub>10</sub> <sup>+</sup>
1-ethyl-1-methylpyrrolidinium	Pyr <sub>2</sub> <sup>+</sup>
1-butyl-1-methylpyrrolidinium	Pyr <sub>4</sub> <sup>+</sup>
1-hexyl-1-methylpyrrolidinium	Pyr <sub>6</sub> <sup>+</sup>
1-methyl-1-octylpyrrolidinium	Pyr <sub>8</sub> <sup>+</sup>
1-decyl-1-methylpyrrolidinium	Pyr <sub>10</sub> <sup>+</sup>
ethylsulfate	S <sub>2</sub> <sup>-</sup>
butylsulfate	S <sub>4</sub> <sup>-</sup>
hexylsulfate	S <sub>6</sub> <sup>-</sup>
octylsulfate	S <sub>8</sub> <sup>-</sup>
decylsulfate	S <sub>10</sub> <sup>-</sup>

<b>Ball class</b>	
tetrafluoroborate	$\text{BF}_4^-$
bromide	$\text{Br}^-$
chloride	$\text{Cl}^-$
tris(pentafluoroethyl)trifluorophosphate	$\text{FEP}^-$
iodide	$\text{I}^-$
hexafluorophosphate	$\text{PF}_6^-$
<b>Teeter-totter class</b>	
trifluoromethanesulfonate	$\text{OTF}^-$
bis(trifluoromethylsulfonyl)imide	$\text{TFSI}^-$
di[bis(trifluoromethanesulfonyl)imide]	$\text{TFSI}_2^-$
<b>Roly-poly class</b>	
tetracyanoborate	$\text{B}(\text{CN})_4^-$
tricyanomethanide	$\text{C}(\text{CN})_3^-$
bis(fluorosulfonyl)imide	$\text{FSI}^-$
dicyanamide	$\text{N}(\text{CN})_2^-$
thiocyanate	$\text{SCN}^-$

**9.2. Table 2.** Structure-determined parameters of the modelled ILEIs with head-tail ions

Ion	$\theta_M [\mu\text{C}\cdot\text{cm}^{-2}]$	$\varphi_M [\text{V}]$	$\varphi_S [\text{V}]$	$C_M [\mu\text{F}\cdot\text{cm}^{-2}]$	$C_S [\mu\text{F}\cdot\text{cm}^{-2}]$	$a$
$\text{AM}_2^+$	125.03	-5.6	-1.6	13.5	22.5	0.60
$\text{AM}_4^+$	98.31	-1.2	-30.1	13.5	22.5	0.60
$\text{AM}_6^+$	93.54	-4.3	-0.7	5.4	21.8	0.25
$\text{AM}_8^+$	89.72	-4.4	-0.6	4.6	20.2	0.23
$\text{AM}_{10}^+$	84.95	-4.5	-0.6	3.7	18.9	0.20
$\text{IM}_2^+$	43.91	-4.6	-1.2	4.9	9.4	0.52
$\text{IM}_4^+$	44.86	-4.1	-1.0	5.4	10.9	0.50
$\text{IM}_6^+$	44.86	-4.0	-1.0	6.2	11.3	0.54
$\text{IM}_8^+$	44.86	-4.1	-1.1	6.2	10.9	0.57
$\text{IM}_{10}^+$	43.91	-3.9	-1.0	5.9	11.3	0.52
$\text{Py}_2^+$	42.95	-3.8	-1.2	8.1	11.3	0.71
$\text{Py}_4^+$	42.95	-3.8	-1.1	7.9	11.3	0.69
$\text{Py}_6^+$	42.95	-3.8	-1.1	7.5	11.3	0.66
$\text{Py}_8^+$	42.95	-3.8	-1.1	7.9	11.3	0.69

$\text{Py}_{10}^+$	42.95	-3.8	-1.1	7.9	11.3	0.69
$\text{Pyr}_2^+$	46.77	-6.9	-2.1	4.6	6.7	0.69
$\text{Pyr}_4^+$	46.77	-6.9	-2.1	4.8	6.7	0.71
$\text{Pyr}_6^+$	44.86	-6.8	-2.2	5.0	6.6	0.75
$\text{Pyr}_8^+$	43.91	-6.5	-2.1	5.2	6.7	0.78
$\text{Pyr}_{10}^+$	46.77	-7.1	-2.3	5.1	6.6	0.77
$\text{S}_2^-$	-70.63	7.7	1.4	2.8	9.1	0.31
$\text{S}_4^-$	-65.86	7.2	1.5	3.5	9.1	0.39
$\text{S}_6^-$	-68.72	7.5	1.7	3.8	9.1	0.42
$\text{S}_8^-$	-68.72	7.5	1.6	3.5	9.1	0.39
$\text{S}_{10}^-$	-68.72	7.5	1.5	3.1	9.1	0.34
$\text{N}_{2214}^+$	43.91	-7.4	-1.6	2.2	5.9	0.95

**Non-exclusive licence to reproduce the thesis and make the thesis public**

I, Xueran Tao  
(author's name)

1. grant the University of Tartu a free permit (non-exclusive licence) to

reproduce, for the purpose of preservation, including for adding to the DSpace digital archives until the expiry of the term of copyright, my thesis

Maximum packing density  
of ions at ionic liquid-electrode interface  
(title of thesis)

supervised by Vladislav Ivanistsev   
(supervisor's name)

2. I grant the University of Tartu a permit to make the thesis specified in point 1 available to the public via the web environment of the University of Tartu, including via the DSpace digital archives, under the Creative Commons licence CC BY NC ND 4.0, which allows, by giving appropriate credit to the author, to reproduce, distribute the work and communicate it to the public, and prohibits the creation of derivative works and any commercial use of the work until the expiry of the term of copyright.
3. I am aware of the fact that the author retains the rights specified in points 1 and 2.
4. I confirm that granting the non-exclusive licence does not infringe other persons' intellectual property rights or rights arising from the personal data protection legislation.

author's name  
dd/mm/yyyy

Xueran Tao  
27/05/2022